NJC

PAPER

View Article Online
View Journal | View Issue

Cite this: *New J. Chem.*, 2025, **49**, 14623

Received 29th May 2025,
Accepted 21st July 2025

DOI: 10.1039/d5nj02247a

rsc.li/njc

Ultrafast charge separation and photostability in PANI/GO/MoO_3 ternary nanocomposites for dual-function solar photocatalysis: enhanced dye degradation and hydrogen evolution under visible light†

Pritam Hait,[a] Rajeev Mehta[b] and Soumen Basu *[a]

Polyaniline-based photocatalysts have attracted attention due to their favourable bandgap (2.7 eV) and significant visible light absorption (∼43%). In this study, a novel ternary nanocomposite, PANI/GO/MoO_3, synthesized *via* oxidative *in situ* polymerization, combining polyaniline (PANI), graphene oxide (GO), and molybdenum trioxide (MoO_3), was presented with different wt/wt%. Comprehensive characterization using XRD, BET, EDS, XPS, PL, and UV-vis-DRS revealed crystallinity, porosity, and superior optical properties. The FESEM image confirmed the porous morphology of PANI, exfoliated GO layers, and MoO_3 nanorods (60–80 nm). Among the composites, 2.5PGMO (GO–MoO_3: 2.5 wt% and PANI: 97.5 wt%) exhibited the highest electron lifetime (0.612 ms), significantly outperforming individual components such as PANI (0.0495 ms), GO (0.023 ms), and MoO_3 (0.022 ms). Photocatalytic activity was validated through both methyl orange (MO) degradation and solar-driven hydrogen production *via* water splitting. The 2.5PGMO composite achieved 98% MO removal and 70% detoxification within 120 minutes, with a reaction rate surpassing that of traditional photocatalysts. Optimal conditions, such as pH, catalyst dosage, and scavenger presence, enhanced performance. The composite shows 85% degradation of the pollutant over five cycles, and stability of the nanocomposite was confirmed by XRD and ICP-OES. In solar hydrogen production, it delivered an apparent quantum efficiency (AQE) of 30.76% using CH_3OH as a sacrificial agent, with nearly 28% AQE under varying pH conditions. This study underscores the PANI/GO/MoO_3 nanocomposite as a promising multifunctional photocatalyst for simultaneous environmental remediation and sustainable hydrogen production, paving the way for advanced solar-driven technologies.

1. Introduction

In the present era, semiconductor-based photocatalysis is essential for addressing the pressing challenges of energy scarcity and environmental pollution.[1] By harnessing solar energy as a clean, abundant, and renewable source, this technology offers several advantages, including high efficiency, eco-friendliness, and cost-effectiveness.[2–4] To date, the majority of efforts have been concentrated on inorganic semiconductors, including TiO_2 and various metal oxides, sulfides, and nitrides.[5] However, titanium dioxide (TiO_2) has limitations, such as a low quantum yield and sensitivity only to UV light around 4% of solar energy due to its wide band gap of roughly 3.2 eV.[6,7] Additionally, TiO_2 is known to have a carcinogenic nature.[8] Hence, there is an imminent demand for the advancement of novel and enhanced visible-light-driven photocatalysts to maximize solar energy exploitation.[9–11]

In the field of photocatalytic applications for photogenerated fuel production and pollutant degradation, organic semiconductors are still relatively underexplored.[12] In recent developments, conductive polymers featuring extensively delocalized π-conjugated electron systems—such as polypyrrole (PPy),

---

[a] *Department of Chemistry and Biochemistry, TIET-Virginia Tech Center of Excellence in Emerging Materials, Thapar Institute of Engineering & Technology, Patiala-147004, India. E-mail: soumen.basu@thapar.edu*

[b] *Department of Chemical Engineering, TIET-Virginia Tech Center of Excellence in Emerging Materials, Thapar Institute of Engineering & Technology, Patiala-147004, India*

† Electronic supplementary information (ESI) available: This article's supplementary information includes chemical details, Information about the Instruments, EDS and elemental mapping, FTIR, BET–BJH plots, Mott–Schottky plots, Phase angle (degree) *vs.* Frequency plots, GC–TCD results of hydrogen generation, GC–MS data, ICP-OES data, and A comparison Table. See DOI: https://doi.org/10.1039/d5nj02247a

polythiophene (PT), and polyaniline (PANI)—have demonstrated promising capabilities in electron transfer mechanisms.[13] These polymers exhibit notable characteristics such as high mobility of charge carriers, exceptional stability, effective hole-transport abilities, significant absorption of visible light, and reduced rates of charge recombination.[14–16] The intriguing properties of PANI have attracted considerable attention among researchers, prompting an exploration of its unique characteristics and potential applications.[17] Polyaniline (PANI) exhibits a unique conjugation mechanism in which benzenoid and quinoid rings dynamically interact, leading to three distinct oxidation states that function as versatile ensembles adaptable to various situations.[18] This conjugation phenomenon underscores PANI's commercial viability, transcending laboratory settings to emerge as a promising candidate for real-world applications across industries.[19] Noteworthy attributes include its high absorption coefficient within the visible spectrum, positioning PANI as a potential star in diverse industrial sectors where efficient energy absorption is crucial.[20] PANI's remarkable protonation reversibility, resembling a dynamic toggling between charged and uncharged states, enhances its versatility and utility in various contexts.[21,22] Furthermore, PANI's excellent redox properties enable proficient electron handling, rendering it advantageous for catalyzing chemical reactions effectively.[23] Additionally, PANI exhibits notable sensitivity as a photocatalyst, particularly in facilitating organic dye interactions, while its superior light and thermal stability contribute to the sustained photocatalytic activity, promoting cleaner and more sustainable processes.[24] In summary, PANI's multifaceted properties, including its unique conjugation mechanism, high absorption coefficient, reversible protonation, redox capabilities, environmental stability, and photocatalytic sensitivity, collectively position it as a compelling material for further scientific exploration and practical applications across diverse sectors.

The scientific and engineering communities have been captivated by graphene oxide. It is composed of carbon atoms arranged in a hexagonal lattice resembling a honeycomb structure.[25] Its exceptional attributes can be delineated as follows: (i) high surface area: graphene oxide exhibits an extraordinarily large surface area despite its nearly two-dimensional structure, providing an expansive platform for chemical reactions to occur;[26] (ii) electron acceptor: graphene oxide readily accepts electrons, thereby impeding the recombination of photogenerated charge carriers and sustaining their activity;[27] (iii) synergistic hybridization: when PANI and graphene oxide are present together, their hybrid structure, often in conjunction with inorganic materials or transition-metal oxides, enhances degradation rates by mitigating electron recombination losses.[28] In summary, the synergistic partnership between PANI and graphene oxide constitutes a formidable alliance, facilitating efficient degradation processes through their coordinated actions. While PANI and GO composites show enhanced photocatalytic activity compared to individual components, their performance may still fall short of expectations, especially when compared to other advanced photocatalytic materials; that's why it is necessary to introduce a metal oxide to form a ternary composite.[29] Much research has verified that enhancing the photocatalytic activity of semiconductor photocatalysts (such as $Bi_2O_2CO_3$, ZnO, TiO_2, CdS, and $Bi_{12}O_{17}C_{l2}$) by sensitizing them with PANI leads to improved reactivity in photocatalysis.[21,22,30–32] In the present study, molybdenum trioxide (MoO_3) is used because of its non-toxicity, thermal stability, cost-effectiveness, and rich oxygen vacancies.[33] Due to its large specific surface area and numerous active sites, it demonstrates outstanding photo-assisted degradation properties. MoO_3 is an n-type semiconductor characterized by a bandgap energy ranging from 2.5 to 3.2 eV.[34] This material exhibits remarkable light absorption capacity in both the visible and UV regions. Moreover, MoO_3 acts as a photocatalyst, demonstrating an impressive adsorption capacity for organic dyes in photocatalytic processes.

In recent decades, substantial research has investigated the photocatalytic properties of titanium dioxide (TiO_2), cadmium oxide (CdO), cadmium selenide (CdSe), zinc oxide nanoparticles (ZnO NPs), and their combinations with conductive polymers (CPs). Researchers have proposed various mechanisms to explain the synergistic effects observed between CPs and metal oxide NPs, such as π to π^* transition of electrons from the highest occupied molecular orbital (HOMO) to the lowest unoccupied molecular orbital (LUMO), increased phase space separation between charge carriers, elevated concentration of hydroxyl free radicals, and enhanced photo-activity under ordinary light.[35] Our main hypothesis of this work is threefold: firstly, presence of rod shaped MoO_3 helps in better dispersion of 2D GO, with a reduction in the number of its stacked layers, and secondly, this will lead to a synergistic improvement in the electron lifetime of the ternary composite of PANI/GO/MoO_3. Thirdly, increased electron lifetime would lead to better dye degradation and greater solar energy hydrogen production *via* water splitting.[36,37]

This study centers on the fabrication of a novel ternary composite comprising polyaniline (PANI), molybdenum trioxide (MoO_3), and graphene oxide (GO) (Scheme 1) to assess its efficacy in the breakdown of the methyl orange (MO) dye through photocatalysis under LED light exposure. The synthesized ternary composites were comprehensively characterized using techniques such as X-ray diffraction (XRD), X-ray photoelectron spectroscopy (XPS), Fourier-transform infrared spectroscopy (FTIR), field-emission scanning electron microscopy (FESEM), electrochemical impedance spectroscopy (EIS), and UV-visible diffuse reflectance spectroscopy (UV-DRS). The study examined several photocatalytic features, such as the amount of catalyst used, the area effectively lit, the pH of the solution, and the impact of scavengers. Analysis of intermediates and degradation products was performed using gas chromatography–mass spectrometry (GC/MS). Furthermore, potential mechanisms of photocatalytic degradation were explored to enhance comprehension of the procedure. Moreover, the photocatalyst demonstrated the capability to generate green hydrogen gas through photocatalytic water splitting. We assessed various conditions such as the presence of a sacrificial agent and acidic, basic, and neutral environments for the hydrogen evolution process. The apparent quantum yield

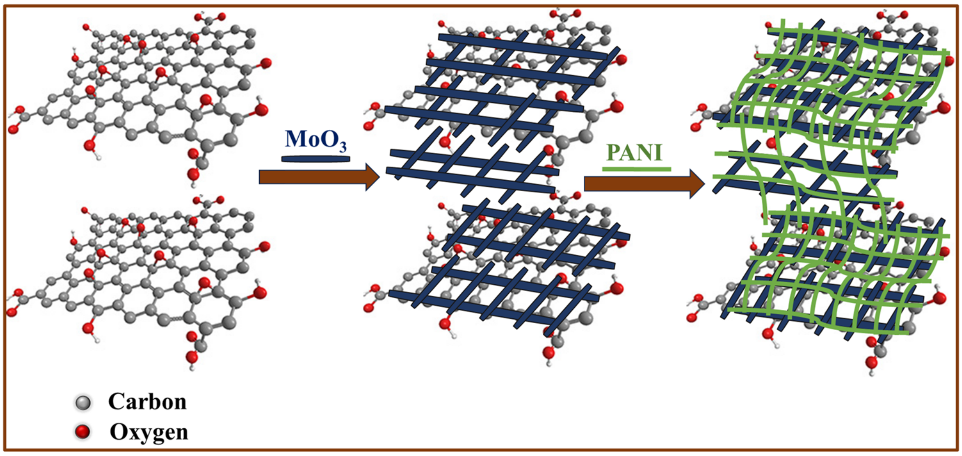

Scheme 1 Dispersion of graphene oxide layers and MoO_3 nanorods, and *in situ* polymerisation of PANI.

(AQE%) for photochemical water splitting was then determined under these conditions. This process entails the catalyst absorbing photons, which initiates chemical processes that break down organic contaminants into less hazardous substances and enable water to split into hydrogen (H_2) and oxygen (O_2).

2. Experimental section

The chemicals employed in the synthesis procedure are detailed in the supplementary materials (S1, ESI†).

2.1. Preparation of MoO_3 and GO

MoO_3 nanoparticles were prepared by dissolving 0.2 M ammonium molybdate in 10 mL of distilled water and then adding 5 mL of concentrated HNO_3. The mixture was subsequently placed into a Teflon-lined stainless-steel autoclave and kept at 150 °C for 12 hours. Afterward, the precipitates were separated, washed, and subjected to vacuum drying at 70 °C for another 12 hours.[38] Graphene oxide was synthesized from the graphite precursor by the modified Hummers method.[39]

2.2. Preparation of the ternary nanocomposite

To commence the process, a composite of GO–MoO_3 in a 1 : 1 ratio was synthesized through an *in situ* procedure utilizing the precursor of MoO_3. Subsequently, various weight percentages of the resulting 1 : 1 GO–MoO_3 composites were employed to fabricate ternary composites using the oxidative polymerization method. The procedure involved introducing 1 : 1 GO–MoO_3 and aniline into a 2 M hydrochloric acid solution, followed by stirring for one hour and additional sonication for another hour. Subsequently, ammonium persulphate (APS) was gradually added, initiating an overnight stirring process for polymerization. The ensuing solution was subjected to thorough washing with 2 M hydrochloric acid and water, and then dried at 60 °C for 24 hours (Scheme S1, ESI†).[20] This method facilitated the preparation of PANI/GO/MoO_3 composites with distinct weight ratios (1, 2.5, and 4), labeled as 1PGMO, 2.5PGMO, and 4PGMO, respectively.

2.3. Characterization methods

The resulting samples were systematically characterized utilizing various analytical techniques, including X-ray diffractometry (XRD), field-emission scanning electron microscopy (FESEM), energy dispersive X-ray spectroscopy (EDS), X-ray photoelectron spectroscopy (XPS), UV-visible spectrophotometry, steady-state photoluminescence (PL), Fourier transform infrared spectroscopy (FTIR), Brunauer–Emmett–Teller (BET), gas chromatography–mass spectrometry (GC–MS), and gas chromatography–thermal conductivity detector (GC–TCD). Comprehensive details about the instruments utilized are available in the ESI† (S2).

2.4. Experiments involving photocatalysis

2.4.1. Test for evaluating the efficacy of photocatalytic degradation. To assess the photocatalytic degradation capability, methyl orange (MO) was chosen as the test compound. In a standard procedure, 4 mg of photocatalyst was introduced into 20 mL of methyl orange aqueous solution (20 ppm). The suspension was kept in the dark for 120 minutes to reach an adsorption–desorption equilibrium. Utilizing a photocatalytic reactor powered by a 40 W LED lamp (Phillips) as the light source, the system was agitated using a magnetic stirrer throughout the entire photocatalytic process. A UV-vis spectrophotometer was employed to measure the remaining concentrations of MO. The percentage (%) of MO degradation was determined using the following formula:

$$\text{Degradation }(\%) = \frac{C_0 - C_t}{C_0} \times 100 \qquad (1)$$

where C_0 and C_t denote the concentrations of MO at the beginning of the experiment (time '0') and after being exposed to light irradiation for a specific duration 't', respectively.

The extent of mineralization was determined using the equation

$$\text{Mineralization }(\%) = \frac{\text{TOC}_{\text{initial}} - \text{TOC}_{\text{final}}}{\text{TOC}_{\text{initial}}} \times 100 \qquad (2)$$

Here, "$\text{TOC}_{\text{initial}}$" denotes the initial total organic carbon (TOC) concentration of MO (measured in mg L^{-1}) prior to the degradation process and "TOC_{final}" denotes the concentration of total organic carbon (TOC) in MO after 120 minutes of degradation.

Moreover, the identification of MO degradation products utilized a GC–MS system. Chemical structures were deduced from their m/z values, with 'm' indicating the molecular mass and 'z' denoting the charge number of the product. Mobile phases for analysis consisted of aqueous solutions containing 0.1% dichloromethane (DCM).

2.4.2. Photocatalytic hydrogen production. The photocatalyst, weighing 2 mg, was evenly distributed in a 20 mL aqueous solution. The solution contained one mL of MeOH as a sacrificial agent. The experiment was conducted under four different conditions: without any sacrificial agent, under acidic conditions, under basic conditions, and with a sacrificial agent in an environment saturated with nitrogen gas. The container was sealed tightly with an airtight cap. Using a photocatalytic reactor equipped with a 40 W LED lamp (Phillips) as the light source, the generated H_2 photoproduct was analyzed using gas chromatography (GC) with a thermal conductivity detector (TCD) and nitrogen as the carrier gas. During the photocatalytic process, the system was stirred continuously using a magnetic stirrer. The following formula was used to calculate the apparent quantum efficiency (AQE):

$$\mathrm{AQE}\ (\%) = \frac{n \times \Delta G}{W \times S \times T} \times 100 \tag{3}$$

where n represents the moles of hydrogen produced per unit volume (moles per liter), ΔG the overall Gibbs free energy of water splitting (237 kJ per mole), W the intensity of light radiation (637 watts per square meter), S the surface area of the reaction vessel (in square meters) and T the duration of the reaction (in seconds).

3. Results and discussion

3.1. Characterisation of the prepared photocatalyst

3.1.1. Spectral characterization. The X-ray diffraction (XRD) pattern presented in Fig. 1a illustrates the characteristics of both the pure bulk nanomaterials and their nanocomposites. Examining the peaks at 2θ values of 12.8°, 25.77°, and 39.09° reveals the corresponding lattice plane of $d(100)$, $d(210)$, and $d(310)$ of MoO_3. These peaks confirm the formation of pure MoO_3 nanomaterials with a hexagonal unit cell (JCPDS NO.: 21-0569).[38] Additionally, the XRD analysis identifies peaks at 2θ = 14.78° (121), 20.45° (310), and 25.08° (003), providing evidence for the presence of PANI. The occurrence of the peak at 25.08° (003) further signifies the polymeric characteristics of PANI.[40] Moreover, the peaks at 11.23° (002) and 42.16° (100) indicate the existence of graphitic graphene oxide.[41] By examining the XRD patterns of the nanocomposites 1PGMO, 2.5PGMO, and 4PGMO, it becomes evident that the peaks corresponding to MoO_3, GO, and PANI persist, confirming the successful incorporation of these components into the nanocomposite structures. In the nanocomposite, the amorphous peak at 2θ = 13.1° may be matched with $d(121)$ of PANI and $d(002)$ of GO, and there is one crystalline peak in the amorphous nanocomposite at 2θ = 32.55° due to crystalline MoO_3. This analysis underscores the potential of the 1PGMO, 2.5PGMO, and 4PGMO catalysts, as their composition aligns with the identified

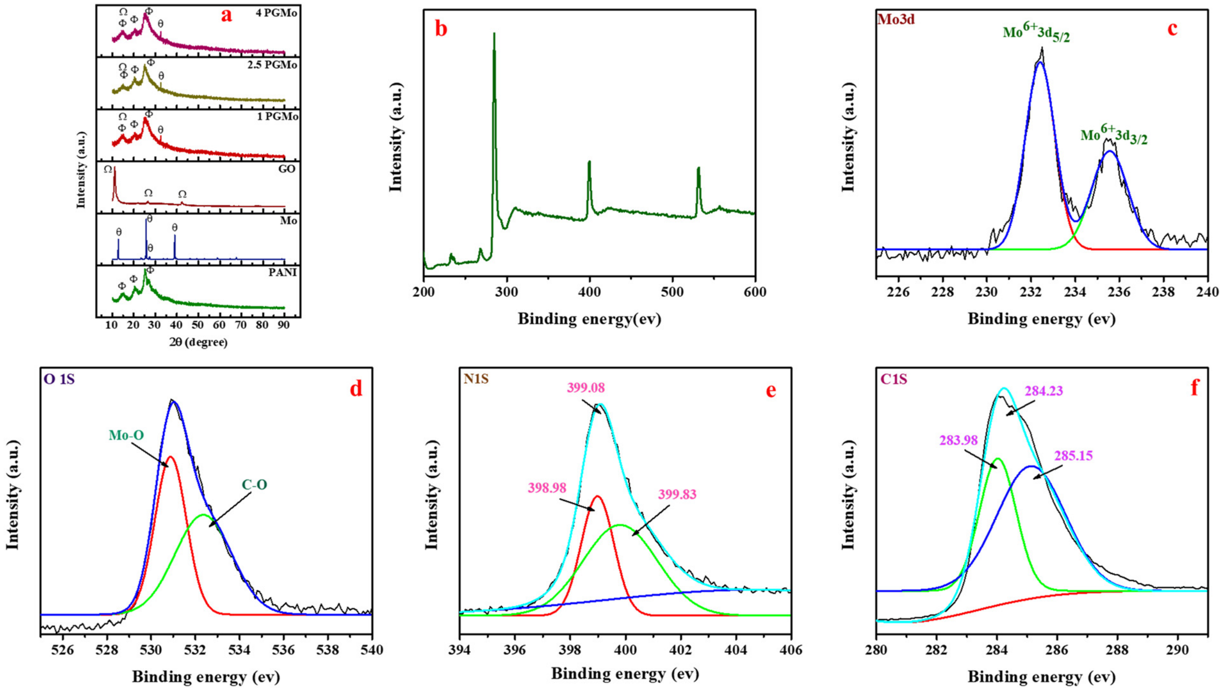

Fig. 1 (a) XRD pattern, (b) XPS survey spectrum of 2.5PGMO, (c) Mo 3d core level spectrum, (d) O 1s core level spectrum, (e) N 1s core level spectrum and (f) C 1s core level spectrum.

characteristics of MoO_3, graphene oxide, and polyaniline. We used the Scherrer equation to determine the average crystallite sizes of MoO_3, PANI, g-GO, and 2.5PGMO. The Scherrer equation is[42]

$$D = \frac{k\lambda}{\beta \cos \beta\theta} \tag{4}$$

The crystallite size (D), calculated using the Scherrer equation, depends on various parameters. Here, k represents the Scherrer constant, while λ stands for the wavelength of the X-ray source, typically 0.15406 nm. Additionally, β refers to the full-width half-maxima (FWHM) measured in radians, and θ denotes the peak position, also in radians. Applying these parameters to the Scherrer equation allows for the determination of the "D" of MoO_3, PANI, g-GO, and 2.5PGMO, which are 60.005 nm, 132.235 nm, 102.65 nm, and 101.34 nm, respectively.

The investigation into the atomic oxidation states of elements within the ternary composite (2.5PGMO) involved XPS. The XPS survey spectrum revealed (Fig. 1b) that the presence of Mo, C, N, and O elements in the ternary composite was conclusively confirmed. To delve deeper into the elemental composition and chemical states, Gaussian fitting was applied to deconvolute the elemental spectra of Mo 3d, C 1s, N 1s, and O 1s. Further, analysis of the Mo 3d spectrum (Fig. 1c) revealed the distinct photoemission peaks at 236.4 eV and 232.5 eV corresponding to Mo^{6+} $3d_{3/2}$ and Mo^{6+} $3d_{5/2}$.[43,44] Examining the C 1s spectrum in Fig. 1f revealed three distinct binding energies representing different carbon bonding states. The peak at 283.98 eV corresponds to carbon atoms bonded to hydrogen (C–H), carbon–carbon bonds (C–C), and carbon–carbon single bonds (C–C), indicating non-oxygenated carbon. The peak at 284.23 eV represents carbon atoms bonded to oxygen (O–C), carbon–oxygen bonds (C–O), and carbon–oxygen single bonds (C–O), indicating oxygenated carbon. Lastly, the peak at 285.15 eV indicates carbon atoms bonded to nitrogen (C–N) and carbon–nitrogen bonds (C–N), indicating nitrogenous carbon.[45,46] Three distinct peaks were observed in the N 1s spectrum (Fig. 1e), each representing different nitrogen environments. The peak at 398.98 eV indicates the presence of the quinoid amine, while the peak at 399.08 eV is associated with the benzenoid amine. Lastly, the peak at 399.83 eV is attributed to the nitrogen cationic radical ($N^{+\bullet}$).[47] This spectral analysis offers valuable insights into the diverse chemical configurations of nitrogen within the synthesized ternary composite (2.5PGMO), shedding light on its molecular structure and potential functionalities. Turning attention to the O 1s spectrum depicted in Fig. 1d, two prominent peaks were identified at 531 eV and 532.2 eV. These peaks were associated with the Mo–O bonds present in the MoO_3 hexagonal structure and the hydroxyl group located on the surface of the composite material.[48] This observation underscores the significance of oxygen in the bonding network of the composite material, highlighting its role in facilitating interactions and structural stability.

The FTIR spectral analysis reveals distinct absorption peaks corresponding to specific vibrational modes and chemical groups within the materials. The peak at 1540 cm^{-1} signifies the C═C stretching vibration mode of the benzenoid ring and the peak at a frequency of 1395 cm^{-1} represents the stretching of the C–N bond within the ring structure. Furthermore, the 1267 cm^{-1} signal indicates the existence of the protonated C–N group. Within the context of conducting polymers, the detection of an absorption peak around 775 cm^{-1} signifies the spread of electrons throughout the polymer matrix.[49,50] Regarding graphene oxide (GO), distinctive peaks are observed in the spectrum. The peak at 3500 cm^{-1} is attributed to the stretching vibration of the O–H bond in GO, while the peak at 1715 cm^{-1} represents carboxylic groups' C═O stretching. Furthermore, the peak identified at 1613 cm^{-1} represents the frequency associated with O–H bending and aromatic C═C stretching. Additionally, the peak at 1383 cm^{-1} indicates the presence of tertiary C–OH bonds. Finally, the peak observed at 1221 cm^{-1} provides evidence for the existence of epoxy C–O groups.[51–54] The distinctive pattern includes a notable small intensity peak, followed by a subsequent high-intensity peak at 838.5 cm^{-1} and 982.9 cm^{-1}, characteristic of the u_s (Mo═O) stretching vibrations associated with the hexagonal phase. Notably, these features in the spectrum are indicative of the specific vibrational modes inherent to the hexagonal crystalline structure. The absorption peaks observed at 476.2 cm^{-1} relate to the vibration of the Mo–O bond. This spectral region captures the unique characteristics of the chemical bonds within the hexagonal MoO_3 structure.[55] The detailed vibrational analysis of other synthesized samples is presented in Fig. S1 (ESI†), enhancing our understanding of the bonding configurations of the material, and providing valuable insights into its structural properties. The successful synthesis of the nanocomposites is confirmed by observing absorption peaks associated with various functional groups. The presence and modified positions of these absorption peaks offer concrete evidence of the effective formation of the desired nanocomposite, providing valuable insights into its chemical composition and structural characteristics.

The ability of photocatalysts to absorb light is crucial for their photocatalytic activity. In Fig. 2a, the UV-vis absorption spectra of the obtained photocatalysts are presented. MoO_3 nanorods exhibit intense absorption in the ultraviolet spectrum (250–400 nm). However, the ternary nanocomposites (PGMO) demonstrate a broader absorption in the UV as well as visible region. This broader absorption is attributed to the presence of PANI, which acts as a sensitizer for visible light. Moreover, the hue of the photocatalysts shifts from white for MoO_3 to dark green for ternary nanocomposites, which indicates the successful incorporation of PANI into the composite structure and reflects its visible light-absorption properties. Consequently, it is anticipated that the ternary nanocomposites will exhibit superior photocatalytic performance compared to pure MoO_3 under visible-light irradiation, owing to their enhanced light-absorption capabilities facilitated by the PANI component.

The energy gap of a semiconductor can be calculated using Tauc's formula, which is expressed as $(\alpha h\nu)^{1/n} = A(h\nu - E_g)$, where $h\nu$ represents the photon energy, E_g is the bandgap value,

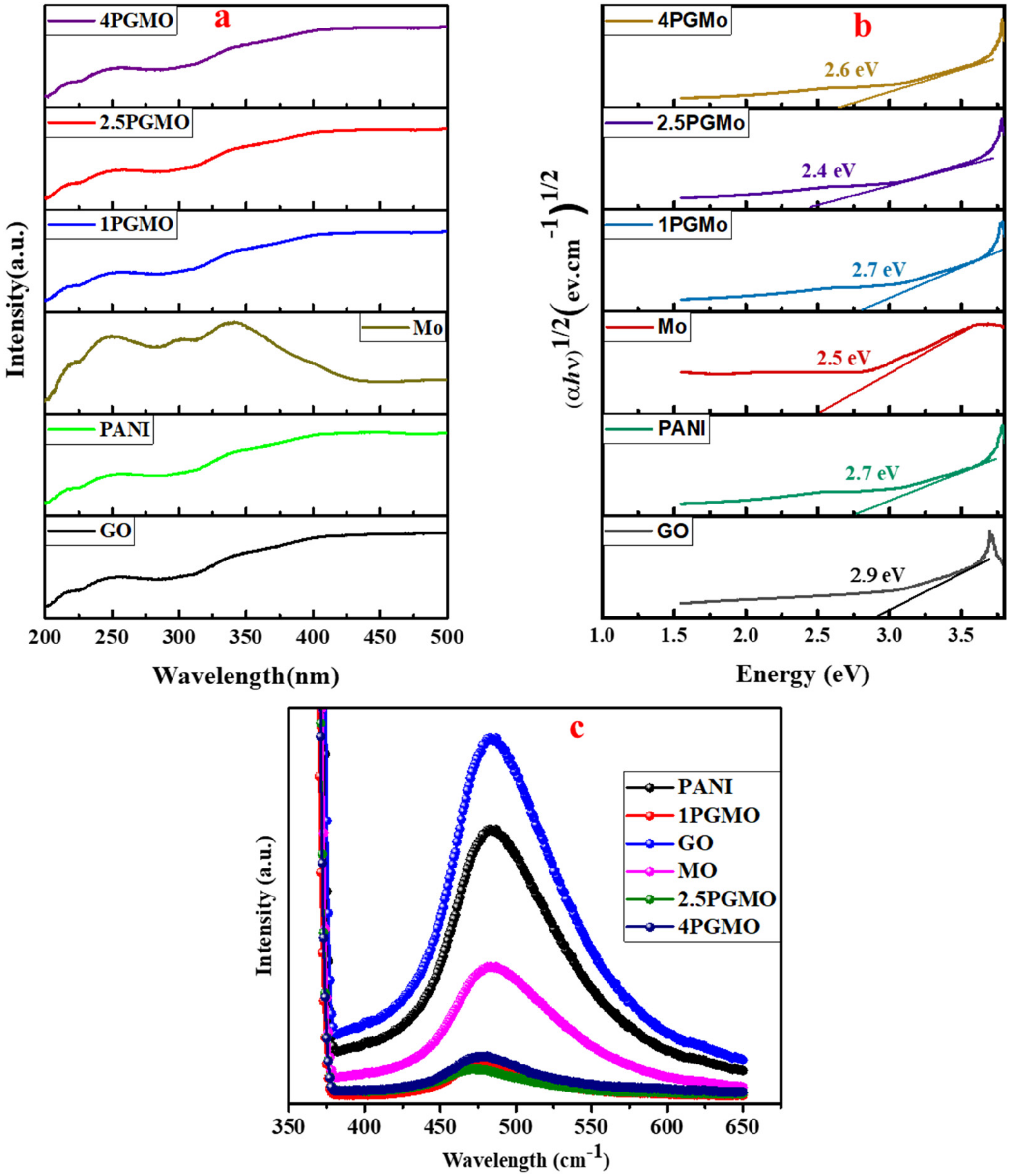

Fig. 2 (a) UV-vis DRS spectra, (b) Tauc's plot, and (c) PL spectra of GO, PANI, MO, 1PGMO, 2.5PGMO, and 4PGMO.

A is the proportionality constant, and α is the optical absorption coefficient. The value of the exponent, denoted as "n", depends on the electronic transition property, with $n = 1/2$ indicating a direct transition and $n = 2$ indicating an indirect transition. In this study, the bandgap energy (E_g) was derived from graphs representing $(\alpha h\nu)^2$ *versus* E_g. As illustrated in Fig. 2b, the E_g of MoO_3 is calculated to be 2.5 eV, while for 2.5PGMO composites, the E_g value is 2.4 eV, for 1PGMO it is 2.7 eV, and for 4PGMO it is 2.64 eV. The decrease in E_g for the 2.5PGMO nanocomposite suggests a significant broadening of the visible light response range after PANI modification. That's why, we use 2.5PGMO for photocatalytic studies. This broadening of the visible light response range indicates that the incorporation of PANI is advantageous for improving the photocatalytic efficiency of MoO_3 in the 2.5PGMO composite.

Typically, photoluminescence (PL) spectra are utilized to assess the effectiveness of processes such as photo-generated carrier capturing, movement, transport, isolation, and recombination. Fig. 2c depicts the PL emission spectra of both pure substances (MoO_3, PANI, GO) and their composites (PGMO). These spectra reveal a luminous peak at approximately 450 nm for photocatalysts. Interestingly, when comparing the PL emission intensity of pure MoO_3, PANI, and GO with that of the PGMO composites, a significant decrease in fluorescence intensity is observed in the case of PGMO composites. This decrease in fluorescence suggests the effective isolation of electron–hole pairs generated by light within the composite structure. The efficient separation and effective management of electron–hole pairs is essential for enhancing the photocatalytic degradation performance of materials. This separation prevents the recombination of electron–hole pairs, enabling more efficient use of these carriers in photocatalytic reactions.

3.1.2. Surface properties. The BET study was conducted to assess the overall surface area, mean pore size, and total pore volume for the individual materials and their composites. This analysis is depicted in Fig. S2 (ESI†) and summarized in Table 1. For both pure substances and their composites, a type IV isotherm was observed, demonstrating the creation of multiple molecular adsorption layers and the process of particles condensing within tiny capillary pores. Furthermore, the BJH plot indicated that each material displayed mesoporous characteristics, with pore diameters below 5 nm. Interestingly, the composite materials exhibited a higher pore volume compared to the bulk materials. Specifically, GO and MoO_3 exhibited much lower surface areas in comparison to the composites and PANI. These findings suggest that PANI plays a pivotal role in augmenting the surface area within the composites. This increased surface area is advantageous for efficient adsorption processes. In summary, the BET analysis offers vital information on the structural characteristics of the materials and emphasizes the notable impact of PANI in improving the overall surface area of the composite materials.

3.1.3. Morphological properties. FESEM analysis (Fig. 3a–d) offers valuable insights into the structural features of the prepared composite. The FESEM image of MoO_3 reveals long nanorods with diameters ranging from 60 to 80 nm. Similarly, the FESEM image of polyaniline (PANI) validates the existence of a fibrous structure characterized by a porous texture. In Fig. 3b, well-agglomerated and scrubbed layers of graphene oxide (GO) are visible, indicating effective dispersion and separation of GO layers. The exfoliation of GO can be attributed to the existence of oxygen-containing functional groups on its surface layers. The nanocomposite forms agglomerates of GO with PANI as a result of the fibrous characteristics of PANI. The FESEM image of the nanocomposite material (Fig. 3c) provides evidence for the simultaneous existence of polyaniline, GO, and MoO_3 nanorods, thereby verifying the successful formation of heterojunction structures. The harmonious composition of the produced nanocomposites was determined by the use of EDS (Fig. S3 ESI†). The EDS analysis verified the concurrent existence of carbon (C), nitrogen (N), molybdenum (Mo), and oxygen (O) in the produced nanocomposite. Furthermore, the element color mappings of the nanocomposite material verify the even dispersion of all elements, a critical factor in improving the photocatalytic characteristics of the composite. Overall, the FESEM and EDS analyses provide comprehensive structural and elemental information, essential for understanding the composition and properties of the synthesized nanocomposites.

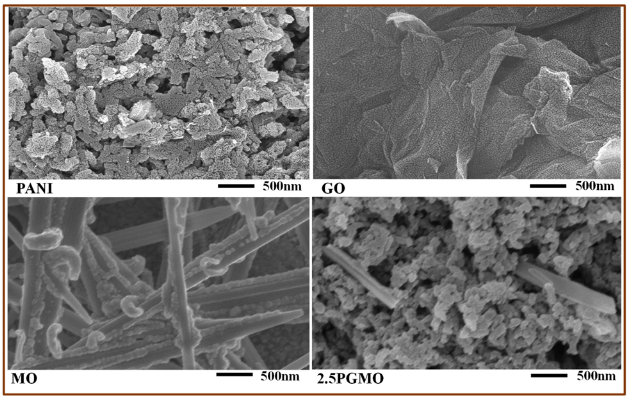

Fig. 3 FESEM image of (a) PANI, (b) GO, (c) MO, and (d) 2.5PGMO.

Table 1 BET surface area, total pore volume, and average pore diameter

Photocatalyst	Surface area (m^2 g^{-1})	Total pore volume (cm^3 g^{-1})	Average pore diameter (nm)
PANI	17.3	0.020	4.7
GO	8.9	0.0172	5
MO	7.4	0.007	3.9
1PGMO	18.9	0.025	3.5
2.5PGMO	29.6	0.034	3.6
4PGMO	27.9	0.022	3.1

3.1.4. Photoelectrochemical measurements. To investigate the photo-electrocatalytic performance, photoelectrochemical measurements were conducted. Employing EIS, a significant tool for studying charge transfer processes at the electrode–electrolyte interface, was instrumental. This method is commonly employed to assess the efficacy of charge separation in photo-induced reactions. The EIS results, illustrated in Fig. 4a–d, depict a representative impedance spectrum of the prepared samples. For a more in-depth analysis, an equivalent circuit (inset in Fig. 4a–d) was applied to interpret the impedance spectra, and EC-Lab software facilitated fitting. In this circuit, R1 represents the system's series resistance. The high-frequency semi-circle indicates the charge-transfer resistance (R^2) at the Pt counter electrode/electrolyte interface, while the middle-frequency semi-circle corresponds to the charge-transfer resistance (R^2) at the anode/electrolyte interface of the sample prepared. In this context, R^3 denotes the charge transfer resistance within the Helmholtz layer, '*C*' denotes chemical capacitance, and '*W*' denotes Warburg impedance. The semi-circular Nyquist plot in Fig. 4 further confirms that the 2.5PGMO composite electrode exhibits a smaller arc radius than pure PANI, GO, and MoO_3 when exposed to visible light. This indicates that the 2.5PGMO photo-electrode demonstrates a more efficient separation of light-induced charge carriers and accelerated interfacial charge transfer. In Fig. S4 (ESI†), the characteristic peak of PANI, GO, MoO_3, and 2.5PGMO shows a frequency of 3214.77 Hz, 6689.46 Hz, 7236.66 Hz, and 259.9 Hz, respectively. This shift to a lower frequency for 2.5PGMO implies a faster process for electron transfer. The relationship between frequency (f) and the duration (τ) of injected electrons' lifespan, as per the equation $\tau \approx 1/(2\pi f)$, suggests that the electron lifetime of 2.5PGMO (0.612 ms) is approximately 12-fold increased compared to that of pure PANI (0.0495 ms), 25-fold increased compared to that of pure GO (0.023 ms), and 28-fold increased compared to that of pure MoO_3 (0.022 ms). This substantial increase indicates a longer injected electron lifetime, effectively inhibiting charge recombination in the

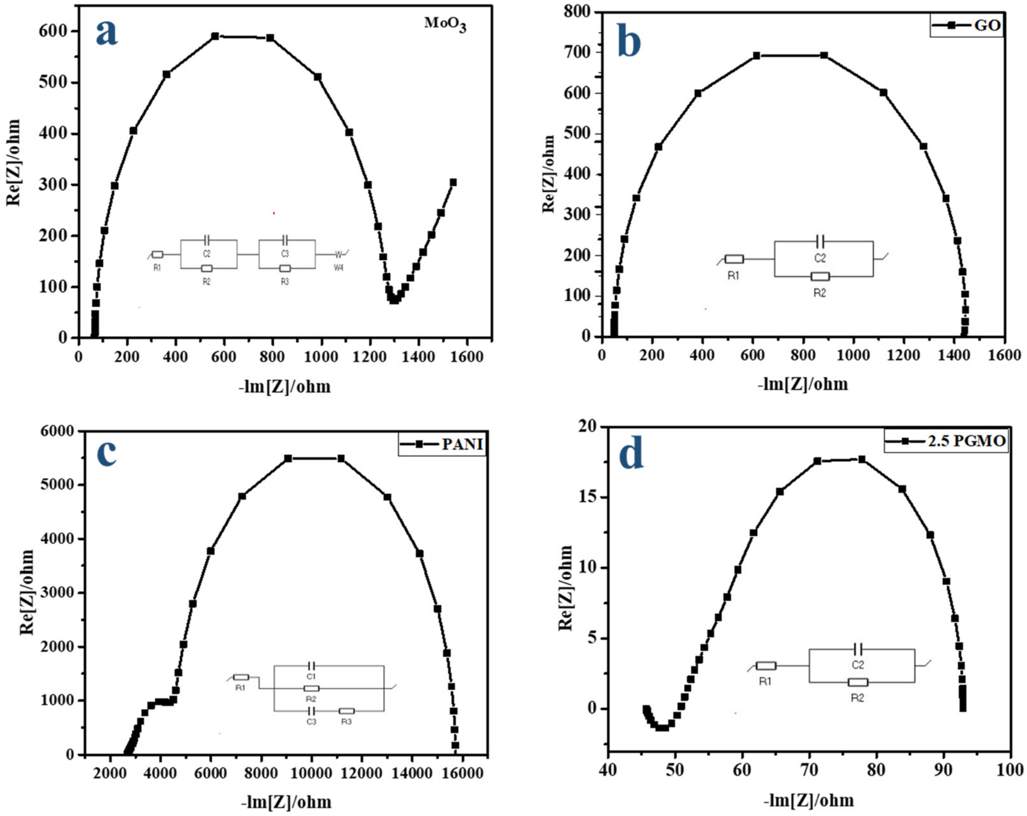

Fig. 4 EIS plot of (a) MoO_3, (b) GO, (c) PANI, and (d) 2.5PGMO.

2.5PGMO photo-electrode. As a result, this improves charge separation efficiency and boosts photo-electrocatalytic performance.

3.1.5. Photocatalytic removal of organic pollutant methyl orange (MO). The efficacy of photolysis, without the presence of catalysts, in removing MO is demonstrated in Fig. 5a. A mere

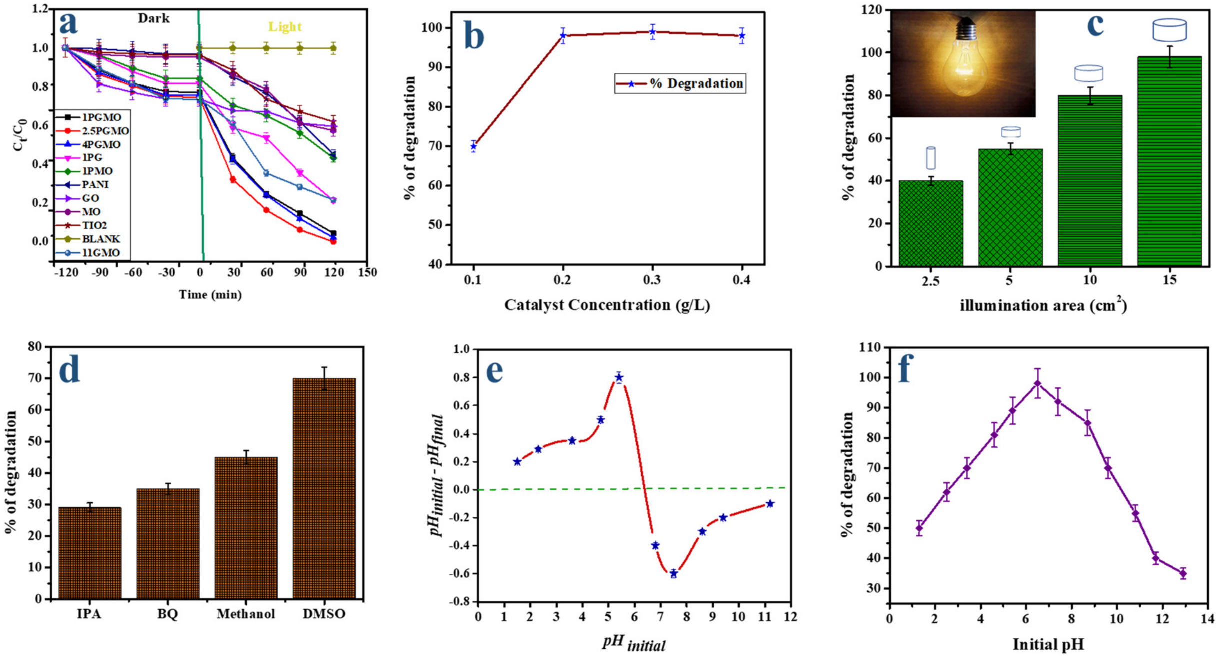

Fig. 5 (a) Kinetic studies, (b) effect of catalyst concentration, (c) impact of illuminated surface area, (d) scavenger studies, (e) pzc studies, and (f) effect of pH on methyl orange solution.

$\sim$3% reduction in absorbance over 120 minutes of exposure to an LED lamp is observed. The poor ability of direct photolysis to degrade verifies the high resistance to deterioration of MO through exposure to light. Upon reaching adsorption–desorption equilibrium in the dark after 120 minutes, approximately 30.2% of MO molecules were adsorbed when using 2.5PGMO; however, bare PANI, GO, molybdenum trioxide, 1PG (99 wt% of polyaniline and 1 wt% of graphene oxide), 11GMO (1 : 1 of graphene oxide and molybdenum trioxide), 1PMO (1 wt% of molybdenum trioxide added to 99 wt% of polyaniline), 1PGMO, 4PGMO, and commercially used TiO_2 samples adsorbed 20.2%, 25.5%, 8.2%, 12.2%, 11.1%, 10.7%, 27.7%, 28.3%, and 7.1% of MO, respectively. The superior adsorption capacity of 2.5PGMO is attributed to the increased surface area with abundant anionic azo dye methyl orange adsorption sites achieved by simultaneously incorporating 2.5 wt% of GO/MO onto the surface of PANI. To enhance removal efficacy, degradation was initiated by light illumination. After 120 minutes of exposure to LED light, the catalytic efficiency associated with the prepared catalysts improved in the following order: PANI (30.1%) < GO (31.2%) < molybdenum trioxide (32.8%) < TiO_2 (33.1%) < 1PMO (45.6%) < 1PG (50.3%) < 11GMO (72.8%) < 1PGMO (85.7%) < 4PGMO (90.4%) < 2.5PGMO (98.9%). These results demonstrate that bare MoO_3 can only decompose a finite quantity of MO due to its limited photo-response spectrum and inadequate specific surface area, and due to rapid recombination of photo-induced e^- and h^+. The presence of PANI and GO species was discovered to enhance the performance. The photocatalytic activity of the composites 1PMO, 1PG, and 11GMO was enhanced compared to the single-component material. However, the degree of degradation was heavily influenced by the loading of GO and MoO_3. The 2.5PGMO composite demonstrated the most effective degradation efficiency for removing MO. However, when the amount of 11GMO was increased to 4 wt%, there was a minor decrease in the effectiveness of MO removal. This behaviour can be attributed to two factors: when the amount of inserted content from 11GMO species was reduced, the photo-generated carriers of charges in the 1PGMO composite materials were not efficiently distributed, leading to a decrease in photodegradability. In addition, the excess presence of 11GMO at a concentration of 4 wt% can obstruct the sites of activity on the catalytic surface, hence hindering the incident irradiation and diminishing the photocatalytic capability. Hence, the inclusion of an optimal quantity of 11GMO species facilitates the attainment of maximum synergy among PANI, GO, and MoO_3, resulting in boosted photocatalytic activity. This enhancement can be credited to a shorter band gap, upgraded light absorption capacity, reduced recombination of electron–hole pairs, and increased absorption ability. Furthermore, a quantitative examination of the photocatalytic disintegration kinetics of MO was conducted by fitting the experimental results to a pseudo-first-order rate equation:

$$\ln(C_t/C_0) = -kt \tag{5}$$

Here, C_0 and C_t refer to the concentrations of MO at 0 and t minutes of irradiation, respectively. The variable k indicates the reaction rate constant (min^{-1}). Fig. S6 (ESI†) illustrates the linear correlation between $\ln(C_t/C_0)$ and reaction time using the prepared catalysts. Remarkably, in line with the degree of decomposition, the degradation rate constant k of different materials can be listed as follows: 1PGMO, 0.02283 min^{-1}; 2.5PGMO, 0.0299 min^{-1}; 4PGMO, 0.02803 min^{-1}; 1PG, 0.01063 min^{-1}; 1PMO, 0.00614 min^{-1}; 11GMO, 0.01073 min^{-1}; PANI, 0.00518 min^{-1}; GO, 0.00174 min^{-1}; MoO_3, 0.00451 min^{-1}; and TiO_2, 0.00385 min^{-1}.

The synergy achieved through the amalgamation of PANI, GO, and MoO_3 was quantified using the synergy factor (R), calculated through the following equation:

$$R = \frac{K_{PANI+GO+MoO_3}}{K_{PANI} + K_{GO} + K_{MoO_3}} \tag{6}$$

where $K_{PANI+GO+MoO_3}$, K_{PANI}, K_{GO}, and K_{MoO_3} denote the rate constants for photodegradation for the PANI/GO/MoO_3 ternary composite, PANI, GO, and MoO_3, respectively. The synergy factors for 1PGMO, 2.5PGMO, 4PGMO, 1PG, 1PMO, and 11GMO were calculated as 1.84, 2.41, 2.26, 1.34, 0.49, and 1.72, respectively. Out of all of the nanocomposites, 2.5PGMO displayed the greatest synergy factor, which resulted in its superior efficacy in degrading photocatalytic substances and a maximum rate constant of 0.0299 min^{-1}.

3.1.6. Impact of the amount of catalyst dosage. The effectiveness of a photocatalyst is significantly influenced by the quantity of catalyst used. To explore the impact of catalyst dosage on the degradation of MO, a set of photocatalytic experiments were conducted, varying the amount of the ternary photocatalyst (2.5PGMO) from 1 to 4 mg while maintaining a constant MO concentration of 20 ppm. When the quantity of photocatalyst was minimal (0.1 g L^{-1}), there was limited involvement of active species in the degradation of MO, resulting in reduced photocatalytic degradation efficiency. The best degradation efficiency was achieved with 0.2 g L^{-1} (Fig. 5b) of the photocatalyst, due to the greater accessibility of active sites and the efficient utilization of light energy. However, an increase in the dosage of the catalyst beyond 0.2 g L^{-1} resulted in no significant change in the degradation rate. This phenomenon can be ascribed to an excessive accumulation of the catalyst, potentially diminishing solution transparency and light penetration ability. In addition, it can deactivate some regions of the catalyst surface that would otherwise be available for the degradation process. In summary, the findings indicate that the maximum amount for MO photodegradation is 0.2 g L^{-1} of the catalyst.

3.1.7. Effect of solution pH. The adsorption capacity of the composite is heavily controlled by the pH of the solution of dye, which in turn has a major impact on the effectiveness of degradation.[56] To fully grasp how the pH of the solution affects the removal of MO dye, solutions with different pH levels were carefully created employing solutions of 0.1 N HCl and 0.1 N NaOH. Solutions with a catalyst-to-dye concentration ratio of 0.2 g L^{-1} were prepared, and the pH values were monitored prior to and following the degradation procedure. Fig. 5e illustrates that the composite 2.5PGMO possesses a point of zero charges (pzc) around pH 6.5. The degradation effectiveness gradually increases from pH 1 to 5, reaching a maximum at a pH of 6.8 (Fig. 5f). In basic solutions, the degradation effectiveness shows a gradual decrease. This observation underscores the crucial role of solution pH in modulating the photocatalytic degradation efficiency of the composite. The trends suggest that the surface charge of the composite, influenced by the pH conditions, significantly affects the adsorption and subsequent degradation of MO dye molecules. The optimal performance is achieved under slightly acidic conditions (pH 6.5), emphasizing the importance of considering solution pH in designing and optimizing photocatalytic processes for effective pollutant removal. The efficiency of degradation decreases gradually in highly alkaline solutions, mainly because of the creation of metal hydroxide precipitates at the surface of the catalyst.

3.1.8. Effect of the illuminated area. The study effectively explored the significance of the illuminated surface area when employing the 2.5PGMO material serving as a photocatalyst under visible light conditions. A solution containing 0.2 g L^{-1} of photocatalyst was mixed with 20 ppm of MO dye. The mixture was agitated under visible light for a duration of 120 minutes. Vessels of varying diameters were used to alter the reaction's surface area while keeping the distance between the pollutant solution's upper surface and the lamp's bottom surface constant at 6 cm. The results demonstrated that as the surface area that was exposed to the reaction mixture increased, there was a commensurate enhancement in the degradation efficiency (Fig. 5c). Increased surface area in the reaction mixture resulted in intensified exposure to light, hence enhancing the photocatalytic breakdown of contaminants and yielding the best efficiency in degradation.

3.1.9. Probable degradation pathway of MO. When examining the intermediates generated while decomposing organic dyes through photodegradation, it is crucial to track the TOC and COD levels in the solution as it undergoes light exposure. Following 120 minutes of exposure to visible light, the TOC and COD reduction efficiencies for MO are observed to be 70% and 81.1%, respectively. Examination of Fig. 8a suggests that the solutions undergo nearly complete mineralization, containing intermediates characterized by a limited mineralization potential. This observation implies a thorough breakdown of the organic dye into byproducts with diminished mineralization capacity.

GC–MS analysis was employed to identify the degradation products of MO through the use of the 2.5PGMO nanocomposite. In S3 (ESI†), the complete mass spectra of MO degradation by 2.5PGMO are presented. The MO dye has a characteristic mass spectrum at *m*/*z* of 306. The mass spectrogram after 120 minutes of degradation (S3, ESI†) shows *m*/*z* peaks at 121, 136, 157, and 172, which match the intermediate products resulting from the degradation of MO. These substances include sulfanilic acid at *m*/*z* 172, which fragments into benzenesulfonic acid at *m*/*z* 157 following the removal of an amino group (NH_2). Additionally, *N*,*N*-dimethyl-*p*-phenylenediamine at *m*/*z* 136 fragments into *N*,*N*-dimethyl benzenenamine at *m*/*z* 121 following the removal of an amino group (NH_2). Based on the results observed, it is suggested that the degradation pathway of MO involves the even division of the azo bond (–N=N–), yielding sulfanilic acid and *N*,*N*-dimethyl-*p*-phenylenediamine.[57] A mechanism of the degradation path is described in Fig. 6. Subsequent degradation of intermediate products may lead to further mineralization into CO_2 and H_2O.

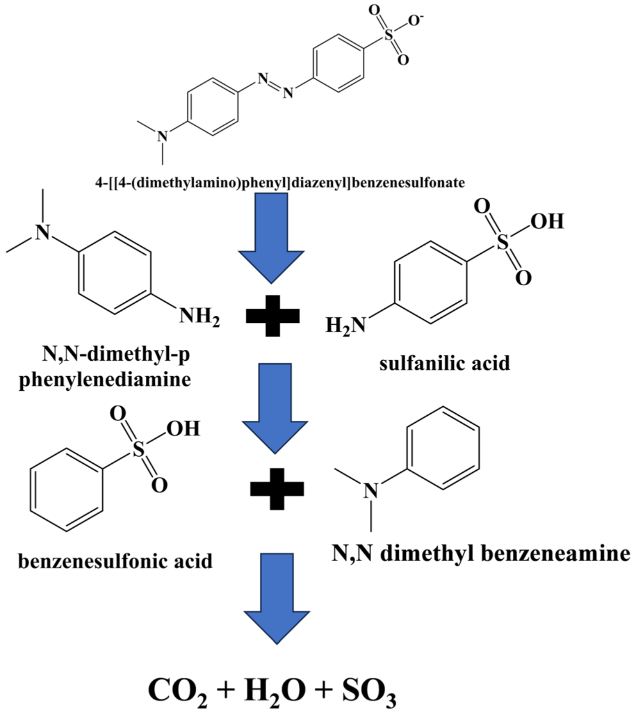

Fig. 6 Potential pathway for photocatalytic degradation of methyl orange using the 2.5PGMO photocatalyst.

3.1.10. Influence of the scavenger and potential mechanisms for charge transfer. The process of degradation primarily engages electrons within the conduction band (CB), holes in the valence band (VB), superoxide radicals, and hydroxyl radicals. All of these factors play a vital function during the degradation process. An investigation into scavenging was conducted to identify the primary species involved in the degradation process. Different scavengers, including isopropyl alcohol (IPA), dimethyl sulfoxide (DMSO), benzoquinone (BQ), and methanol, were employed to capture hydroxyl radicals ($OH^\bullet$), electrons ($e^\bullet$), and superoxide radicals ($O_2^{\bullet-}$) during the degradation process. The scavenger study revealed noteworthy interactions, where the hydroxyl radicals ($OH^\bullet$) acted as reductive agents and interacted with benzoquinone (BQ) to generate hydroquinone. Furthermore, the involvement of DMSO highlights the significant role of hydroxyl radicals ($^\bullet OH$) in the degradation process. The presence of unpaired electrons, along with DMSO's ability to engage in electron transfer through its oxygen atoms, promotes the formation of hydrogen bonds with the hydrogen atoms of hydroxyl radicals

($^{\bullet}$OH).[58] The results depicted in Fig. 5d demonstrate that the process of degradation reaction is significantly affected by methanol, IPA, and BQ. This observation strongly suggests that holes, hydroxyl radicals, and superoxide radicals are the predominant species driving the mechanism of degradation. The comprehensive scavenger study sheds light on the intricate charge transfer mechanisms and the significant roles played by specific reactive species in the overall degradation process. The enhanced performance of the 2.5PGMO composite is attributed to the augmentation of charge separation achieved by incorporating GO and MoO_3 into the polyaniline matrix. To elucidate the mechanism underlying the heightened photocatalytic activity of the 2.5PGMO composite, the relative positions of the bands of PANI, GO, and MoO_3 were determined. In Fig. S5 (ESI†), the Mott–Schottky plots for PANI, GO, MoO_3, and 2.5PGMO reveal their characteristic nature as typical p-type semiconductors, with overall negative slopes.[59] The determination of flat-band potentials, derived from the points where the linear region intersects the *x*-axis, yields values of −0.1 V for PANI, 0.26 V for GO, 0.22 V for MoO_3, and −0.3 V for 2.5PGMO, referenced against Ag/AgCl. Significantly, the ECB of the 2.5PGMO composite displays a substantial negative shift of 0.3 V in comparison to the pure GO and MoO_3. This observed shift can be attributed to electronic interactions involving PANI, GO, and MoO_3, leading to a pronounced lowering of the conduction band potential. This, in turn, results in occupying a conduction band at a high energy level, enhancing the reductive capacity of the 2.5PGMO composite. The detailed analysis of Mott–Schottky plots and band potential shifts sheds light on the underlying electronic interactions and contributes to the understanding of the enhanced photocatalytic properties of the 2.5PGMO composite. In the context of the two channels for the transfer of charges and analysis of energy levels under visible light illumination (Fig. S5, ESI†), the absorption of photons by GO, MoO_3, and PANI is instrumental in generating electrons in the conduction band (CB) of GO and MoO_3, and in the lowest unoccupied molecular orbital (LUMO) of PANI. Simultaneously, this process leaves holes in the valence band (VB) of GO and MoO_3, and in the highest occupied molecular orbital (HOMO) of PANI. Following the principle of energy minimization, electrons from the CB of GO and MoO_3 are more prone to move toward the HOMO of PANI, compared to their transition across the heterojunction barrier from an excited state to a ground state (VB) of GO or MoO_3. At the same time, the generated holes in the HOMO of PANI can attain a potential of $^{-}OH/^{\bullet}OH$ (+2.4 V),[60] while the existing electrons in the CB of GO can reach the $O_2/^{\bullet}O^{2-}$ potentials (−0.046 V).[60] Consequently, these holes (h^+) can efficiently oxidize OH^- to $^{\bullet}OH$, and the electrons (e^-) can reduce O_2 to $^{\bullet}O^{2-}$, both of which are energetic species capable of degrading methyl orange (MO) into by-products. However, it is noted that the existing electrons in the CB of GO and MoO_3 cannot reach the potentials of $O_2/^{\bullet}O^{2-}$ (−0.046 V). Therefore, these electrons directly oxidize MO into degradation products and can produce hydrogen by water splitting. Consequently, $^{\bullet}O^{2-}$, $^{\bullet}OH$, and e^- emerge as the primary active species that catalyze the decomposition of the MO solution into products on the photocatalyst's surface. This outcome aligns with the findings of radical scavenging experiments, suggesting that the charge transfer channel of the catalyst adheres to the direct *Z*-scheme mechanism (Fig. 7). The following summary encapsulates the key points:

$$\mathrm{PANI} + h\nu \rightarrow e^-_{\mathrm{LUMO}}\,(\mathrm{PANI}) + h^+_{\mathrm{HOMO}}\,(\mathrm{PANI}) \tag{7}$$

$$\mathrm{GO} + h\nu \rightarrow e^-_{\mathrm{CB}}\,(\mathrm{GO}) + h^+_{\mathrm{VB}}\,(\mathrm{GO}) \tag{8}$$

$$\mathrm{MoO_3} + h\nu \rightarrow e^-_{\mathrm{CB}}\,(\mathrm{MoO_3}) + h^+_{\mathrm{VB}}\,(\mathrm{MoO_3}) \tag{9}$$

$$e^-_{\mathrm{LUMO}}\,(\mathrm{PANI}) + \mathrm{O_2} \rightarrow {}^{\bullet}\mathrm{O}^{2-}\,(\mathrm{PANI}) \tag{10}$$

$$h^+_{\mathrm{VB}}\,(\mathrm{PANI/GO/MoO_3}) + \mathrm{OH}^- \rightarrow {}^{\bullet}\mathrm{OH}\,(\mathrm{PANI/GO/MoO_3}) \tag{11}$$

$$\mathrm{O}^{2-}\,(\mathrm{PANI}),\ {}^{\bullet}\mathrm{OH}\,(\mathrm{PANI/GO/MoO_3}) + \mathrm{MO} \rightarrow \text{degraded products} \tag{12}$$

3.1.11. Reusability studies. The durability of the photocatalyst is a critical factor for the ongoing utilization of a material used in environmental remediation. Hence, it is crucial to investigate the longevity of the photocatalytic composite under multiple cycles of photodegradation. The findings indicated that the 2.5PGMO composite demonstrated remarkable photostability, as evidenced by the high degradation efficiency of 85–98% for MO even after undergoing five cycles. This is depicted in the graphs depicting photodegradation presented in Fig. 8b. After undergoing five cycles, the nanocomposite was analyzed using XRD analysis. The results indicated a slight reduction in peak intensity, likely because of the adsorption of dye molecules at the surface of the catalyst. However, there was no alteration observed in the catalyst's XRD pattern (Fig. 8d). ICP-OES analysis (Table S2, ESI†) indicated a very low concentration of molybdenum metal (0.01 ppm) in the sample after degradation, which was produced by utilizing a catalyst quantity of 0.2 g L^{-1} for degradation. Since the World Health Organization stated that this level of metal consumption poses no harm to the human body, we decided against conducting a toxicity analysis. This suggests that the photocatalyst maintains its durability and integrity over time.

A comparison was conducted between the 2.5PGMO photocatalyst and other materials that have been reported in the literature for the photocatalytic purification of organic pollutants. The results are organized in Table S3 (ESI†). The results of the investigation show that treating persistent organic pollutants with a lower catalyst concentration works well.

3.1.12. Photocatalytic hydrogen generation studies. The process of generating hydrogen through photocatalytic water splitting under UV light for 24 hours was conducted, employing four distinct water solutions. The starting solution comprised 1 mL of methanol (used as a sacrificial agent) mixed with 19 mL of water. The second solution entailed the process of combining 1 mL of HCl diluted with 19 mL of water, which led to the formation of an acidic solution. The third solution was prepared by combining 1 mL of 1 N NaOH diluted with 19 mL of water, resulting in a basic solution. The fourth solution

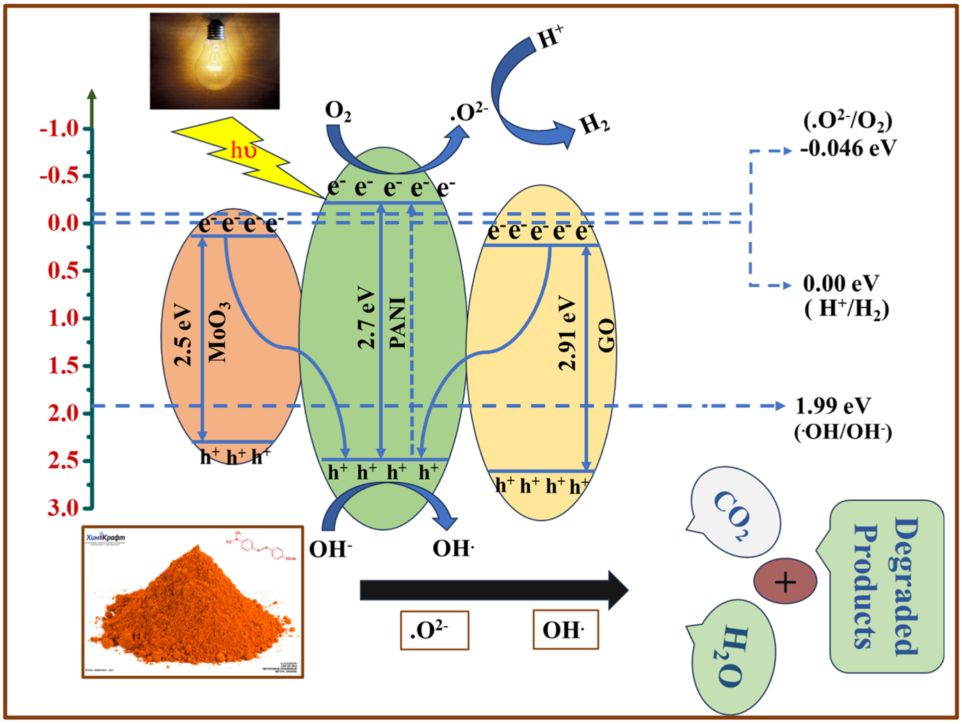

Fig. 7 Potential mechanism for the transfer of charges in the process of photocatalytic degradation and hydrogen production.

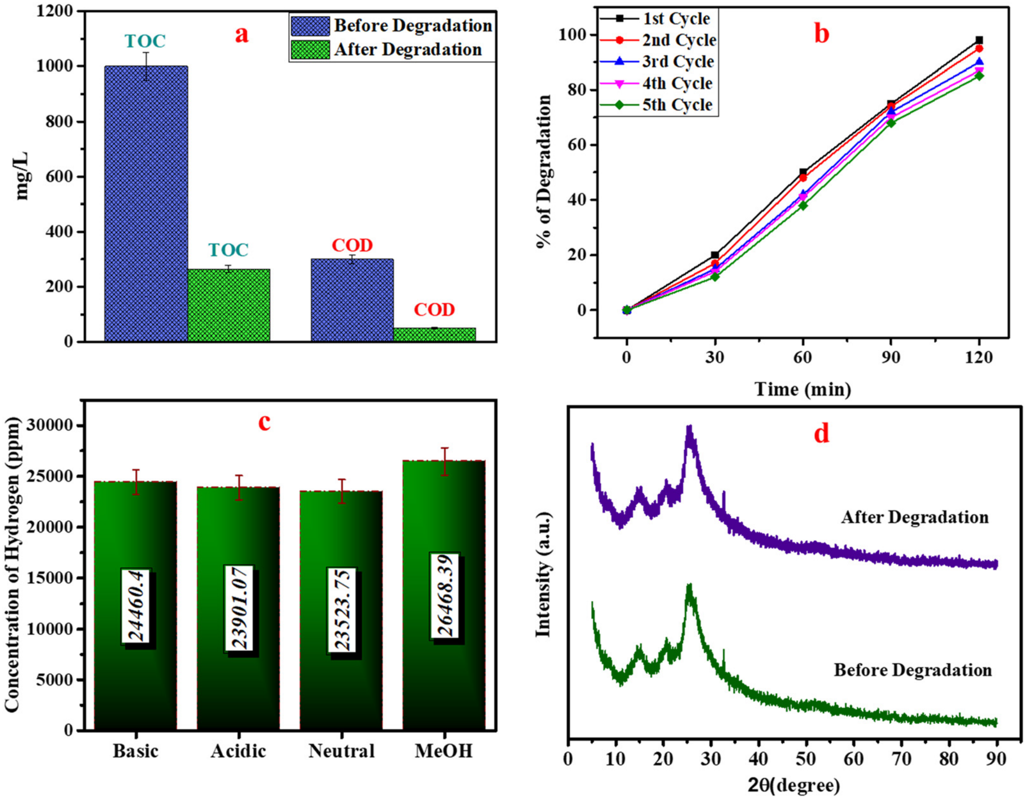

Fig. 8 (a) TOC and COD of MO before and after degradation, (b) reusability studies, (c) hydrogen production studies, and (d) XRD of 2.5PGMO before and after degradation.

consisted of 20 mL of H_2O only. When methanol was present, a total of 26 468.4 ppm of hydrogen gas was released (Fig. 8c). Methanol acts as both a scavenger for holes and a sacrificial donor, leading to the generation of intermediate substances formed during the process like formic acid or formaldehyde.[61] During the water-splitting reaction, hydrogen ions (H^+) generated are partially involved in the photocatalytic reduction process with the aid of these intermediate products. Under acidic conditions, approximately 23 901.07 ppm of hydrogen gas was produced, while under basic conditions, about 24 460.4 ppm of gas consisting of hydrogen was produced. Additionally, in the presence of catalyst and water, around 23 523.75 ppm of hydrogen was produced. The quantum efficiency was approximately 30.76% when using the sacrificial agent, 27.78% in the acidic solution, 28.37% in the basic solution, and 27.34% when using only the catalyst. Eqn (13)–(16) demonstrate how the pairs of electrons and holes within the conduction band and valence band facilitate the redox reaction.[62,63]

Under acidic conditions:

Oxidation:

$$2H_2O\ (l) + 4h^+ \rightarrow O_2\ (g) + 4H^+\ (aq) \quad E^0_{\text{oxidation}} = -1.23\ \text{V} \tag{13}$$

Reduction

$$2H^+ + 2e^- \rightarrow O_2\ (g) + 2H_2\ (g) \quad E^0_{\text{reduction}} = 0\ \text{V} \tag{14}$$

Under basic conditions:

Oxidation:

$$2OH^-(aq) \rightarrow \frac{1}{2}O_2(g) + H_2O(l) + 2e^- \tag{15}$$

Reduction:

$$2H_2O\ (l) + 2e^- \rightarrow H_2\ (g) + 2OH^- \tag{16}$$

Observations from the scavenger study revealed that the photocatalytic activity owes its effectiveness to both electron and hole participation. Consequently, substantial hydrogen production occurred under conditions of both acidity and alkalinity.

4. Conclusion

Ternary nanocomposites, PANI/GO/MoO_3, featuring varied GO–MoO_3 ratios, were synthesized through an *in situ* oxidative polymerization process. Characterization techniques confirmed the synthesis of PANI, GO, and MoO_3, and their unique composites. The aforementioned components were utilized for the purpose of MO mineralization and photocatalytic water splitting, while a sacrificial agent was present. These processes were carried out under both acidic and basic conditions, as well as with the catalyst alone. The electron lifetime of the 2.5PGMO composite stands at 0.612 ms, marking a significant increase compared to PANI, which has a lifetime of 0.0495 ms, GO with 0.023 ms, and MoO_3 with 0.022 ms. Specifically, the electron lifetime of 2.5PGMO is 12 times longer than that of PANI, 25 times longer than that of GO, and 28 times longer than that of MoO_3. The composite's synergistic effect involving MoO_3, PANI, and GO significantly enhanced the efficiency of photocatalytic degradation when exposed to LED light. Notably, among the various composites, 2.5PGMO demonstrated the most promising catalytic activity under light exposure, boasting a first-order rate constant ($0.0299\ \text{min}^{-1}$) that surpassed that of PANI, GO, MoO_3, and TiO_2-P25 by 4.87 times, 17.18 times, 6.63 times, and 7.77 times, respectively. Investigation into how catalyst concentration, size of the illuminated area, and solution acidity affect photodegradation was a focal point of the study. This underscores the pivotal role of h^+, $OH^{\bullet}$, and e^- in the degradation mechanism. The findings demonstrated that using a small quantity of photocatalyst ($0.2\ \text{g L}^{-1}$) achieved 70% mineralization of the MO solution. Moreover, the apparent quantum efficiency (AQE) for photocatalytic hydrogen production was found to be 30.76% when using CH_3OH as the sacrificial agent, 27.78% under acidic conditions, 28.37% under basic conditions, and 27.34% when using only the catalyst. The rod-shaped MoO_3 enhances 2D GO dispersion, reducing its stacked layers and synergistically improving electron lifetime in the PANI/GO/MoO_3 composite. This increased electron lifetime boosts dye degradation efficiency and solar-driven hydrogen production *via* water splitting. This study introduces PANI/GO/MoO_3 as a novel ternary composite with potential applications in diverse solar-powered systems.

Author contributions

Pritam Hait: visualization, writing – original draft. Rajeev Mehta: supervision. Soumen Basu: supervision.

Conflicts of interest

The authors have disclosed that they have no conflicts of interest regarding the conduct of this study and the publication of its findings.

Data availability

The data generated and/or analyzed during the current study are available from the corresponding author upon reasonable request.

Acknowledgements

We gratefully acknowledge the fellowship funding provided by the TIET-Virginia Tech Center of Excellence in Emerging Materials, India. We also extend our gratitude to DCBC and DPMS TIET for providing us characterization facility, and we are also thankful to Dr Akansha Mehta and Prof. O. P. Pandey for XPS characterization and EIS, respectively.

References

1 M. N. Chong, B. Jin, C. W. K. Chow and C. Saint, *Water Res.*, 2010, **44**, 2997–3027.

2 R. Daghrir, P. Drogui and D. Robert, *Ind. Eng. Chem. Res.*, 2013, **52**, 3581–3599.

3 A. Mehtab, S. A. Ali, I. Sadiq, S. Shaheen, H. Khan, M. Fazil, N. A. Pandit, F. Naaz and T. Ahmad, *ACS Sustainable Resour. Manag.*, 2024, **1**, 604–620.

4 R. Gupta, S. A. Ali, Upma, T. Ahmad and R. Gupta, *ACS Appl. Mater. Interfaces*, 2025, **17**, 28244–28255.

5 X. Wang, W. Yang, F. Li, Y. Xue, R. Liu and Y. Hao, *Ind. Eng. Chem. Res.*, 2013, **52**, 17140–17150.

6 X. Chen and W. Shangguan, *Front. Energy*, 2013, **7**, 111–118.

7 A. Kudo, K. Omori and H. Kato, *J. Am. Chem. Soc.*, 1999, **121**, 11459–11467.

8 H. M. Braakhuis, I. Gosens, M. B. Heringa, A. G. Oomen, R. J. Vandebriel, M. Groenewold and F. R. Cassee, *Annu. Rev. Pharmacol. Toxicol.*, 2021, **61**, 203–223.

9 N. Bagherlou, E. Ghasemi, P. Gharbani, M. Babazadeh and A. Mehrizad, *npj Clean Water*, 2024, **7**, 2.

10 A. Mehrizad and P. Gharbani, *Photochem. Photobiol.*, 2017, **93**, 1178–1186.

11 A. G. Khosroshahi and A. Mehrizad, *J. Mol. Liq.*, 2019, **275**, 629–637.

12 X. Wang, K. Maeda, A. Thomas, K. Takanabe, G. Xin, J. M. Carlsson, K. Domen and M. Antonietti, *Nat. Mater.*, 2009, **8**, 76–80.

13 Y. Zheng, L. Lin, B. Wang and X. Wang, *Angew. Chem., Int. Ed.*, 2015, **54**, 12868–12884.

14 G. Yu, J. Gao, J. C. Hummelen, F. Wudl and A. J. Heeger, *Science*, 1995, **270**, 1789–1791.

15 K. Vinodgopal, D. E. Wynkoop and P. V. Kamat, *Environ. Sci. Technol.*, 1996, **30**, 1660–1666.

16 G. Williams, B. Seger and P. V. Kamat, *ACS Nano*, 2008, **2**, 1487–1491.

17 L. Cai, H. Jiang and L. Wang, *Appl. Surf. Sci.*, 2017, **420**, 43–52.

18 M. Nandi, R. Gangopadhyay and A. Bhaumik, *Microporous Mesoporous Mater.*, 2008, **109**, 239–247.

19 X. Ma, H. Li, T. Liu, S. Du, Q. Qiang, Y. Wang, S. Yin and T. Sato, *Appl. Catal., B*, 2017, **201**, 348–358.

20 P. Hait, R. Mehta and S. Basu, *J. Cleaner Prod.*, 2023, **424**, 138851.

21 Z. Zhao, Y. Zhou, F. Wang, K. Zhang, S. Yu and K. Cao, *ACS Appl. Mater. Interfaces*, 2015, **7**, 730–737.

22 Z. Pei, L. Ding, M. Lu, Z. Fan, S. Weng, J. Hu and P. Liu, *J. Phys. Chem. C*, 2014, **118**, 9570–9577.

23 E. Kang, *Prog. Polym. Sci.*, 1998, **23**, 277–324.

24 H. Huang, Y. Liu, S.-T. Lee and Z. Kang, *J. Mater. Chem.*, 2012, **22**, 337–340.

25 S. Dong, X. Ding, T. Guo, X. Yue, X. Han and J. Sun, *Chem. Eng. J.*, 2017, **316**, 778–789.

26 H. Yang, X. Liu, S. Sun, Y. Nie, H. Wu, T. Yang, S. Zheng and S. Lin, *Mater. Res. Bull.*, 2016, **78**, 112–118.

27 S. Dong, Y. Cui, Y. Wang, Y. Li, L. Hu, J. Sun and J. Sun, *Chem. Eng. J.*, 2014, **249**, 102–110.

28 C. Yu, S. Dong, J. Zhao, X. Han, J. Wang and J. Sun, *J. Alloys Compd.*, 2016, **677**, 219–227.

29 J. Miao, A. Xie, S. Li, F. Huang, J. Cao and Y. Shen, *Appl. Surf. Sci.*, 2016, **360**, 594–600.

30 Y. Lin, D. Li, J. Hu, G. Xiao, J. Wang, W. Li and X. Fu, *J. Phys. Chem. C*, 2012, **116**, 5764–5772.

31 C. Wang, L. Wang, J. Jin, J. Liu, Y. Li, M. Wu, L. Chen, B. Wang, X. Yang and B.-L. Su, *Appl. Catal., B*, 2016, **188**, 351–359.

32 Y. Xu, Y. Ma, X. Ji, S. Huang, J. Xia, M. Xie, J. Yan, H. Xu and H. Li, *Appl. Surf. Sci.*, 2019, **464**, 552–561.

33 S. Zaleski, A. J. Wilson, M. Mattei, X. Chen, G. Goubert, M. F. Cardinal, K. A. Willets and R. P. Van Duyne, *Acc. Chem. Res.*, 2016, **49**, 2023–2030.

34 T. He and J. Yao, *J. Photochem. Photobiol., C*, 2003, **4**, 125–143.

35 Y. S. Negi and P. V. Adhyapak, *J. Macromol. Sci. Part C Polym. Rev.*, 2002, **42**, 35–53.

36 S. A. Ali and T. Ahmad, *Small*, 2024, **20**(48), 2403401.

37 S. A. Ali, S. Majumdar, P. K. Chowdhury, S. M. Alshehri and T. Ahmad, *ACS Appl. Energy Mater.*, 2024, **7**, 7325–7337.

38 A. Chithambararaj and A. C. Bose, *J. Alloys Compd.*, 2011, **509**, 8105–8110.

39 Z. B. Siddique, S. Basu and P. Basak, *IEEE Trans. Dielectr. Electr. Insul.*, 2022, **29**, 378–385.

40 P. Ahuja, S. K. Ujjain, I. Arora and M. Samim, *ACS Omega*, 2018, **3**, 7846–7855.

41 H. Shin, K. K. Kim, A. Benayad, S. Yoon, H. K. Park, I. Jung, M. H. Jin, H. Jeong, J. M. Kim, J. Choi and Y. H. Lee, *Adv. Funct. Mater.*, 2009, **19**, 1987–1992.

42 P. Bindu and S. Thomas, *J. Theor. Appl. Phys.*, 2014, **8**, 123–134.

43 M. Morales-Luna, S. A. Tomás, M. A. Arvizu, M. Pérez-González and E. Campos-Gonzalez, *J. Alloys Compd.*, 2017, **722**, 938–945.

44 M. Mihalev, C. Hardalov, C. Christov, M. Michailov, B. Ranguelov and H. Leiste, *J. Phys. Conf. Ser.*, 2014, **514**, 012022.

45 H. Liu, Y. Su, Z. Chen, Z. Jin and Y. Wang, *J. Hazard. Mater.*, 2014, **266**, 75–83.

46 S. Shahabuddin, N. M. Sarih, F. H. Ismail, M. M. Shahid and N. M. Huang, *RSC Adv.*, 2015, **5**, 83857–83867.

47 K. Zhang, L. L. Zhang, X. S. Zhao and J. Wu, *Chem. Mater.*, 2010, **22**, 1392–1401.

48 G. Yang, F. Feng, Y. Luo, J. Qin, F. Yuan, S. Wang, S. Luo and J. Ma, *J. Environ. Chem. Eng.*, 2021, **9**, 106309.

49 A. Abdolahi, E. Hamzah, Z. Ibrahim and S. Hashim, *Materials*, 2012, **5**, 1487–1494.

50 G. Gaikwad, P. Patil, D. Patil and J. Naik, *Mater. Sci. Eng. B*, 2017, **218**, 14–22.

51 C.-M. Chen, Q. Zhang, M.-G. Yang, C.-H. Huang, Y.-G. Yang and M.-Z. Wang, *Carbon*, 2012, **50**, 3572–3584.

52 T. Szabó, E. Tombácz, E. Illés and I. Dékány, *Carbon*, 2006, **44**, 537–545.

53 Y. Fu and X. Wang, *Ind. Eng. Chem. Res.*, 2011, **50**, 7210–7218.

54 P. Wang, J. Wang, X. Wang, H. Yu, J. Yu, M. Lei and Y. Wang, *Appl. Catal., B*, 2013, **132–133**, 452–459.

55 Y.-H. Choi, *Materials*, 2022, **15**, 2182.

56 A. Kumar, R. Kumar and G. Pandey, *Macromol. Symp.*, 2018, **379**(1), 1600192.

57 M. Kgatle, K. Sikhwivhilu, G. Ndlovu and N. Moloto, *Catalysts*, 2021, **11**, 428.

58 A. Kundu, S. Sharma and S. Basu, *J. Phys. Chem. Solids*, 2021, **154**, 110064.

59 Y. Xu, Y. Ma, H. Ji, S. Huang, M. Xie, Y. Zhao, H. Xu and H. Li, *J. Colloid Interface Sci.*, 2019, **537**, 101–111.

60 P. S. Rao and E. Hayon, *J. Phys. Chem.*, 1975, **79**, 397–402.

61 R. A. Rather, S. Singh and B. Pal, *J. Ind. Eng. Chem.*, 2016, **37**, 288–294.

62 T. Jafari, E. Moharreri, A. Amin, R. Miao, W. Song and S. Suib, *Molecules*, 2016, **21**, 900.

63 A. A. Murashkina, T. V. Bakiev, Y. M. Artemev, A. V. Rudakova, A. V. Emeline and D. W. Bahnemann, *Catalysts*, 2019, **9**, 999.